ACS APPLIED MATERIALS & INTERFACES

www.acsami.org

Research Article

One-Step Preparation of High-Stability $CsPbX_3/CsPb_2X_5$ Composite Microplates with Tunable Emission

Chen Zhang, Zeyu Wang,* Zheyuan Da, Jindou Shi, Junnan Wang, Youlong Xu, Nikolai V. Gaponenko, Arshad Saleem Bhatti, and Minqiang Wang*

Cite This: *ACS Appl. Mater. Interfaces* 2024, 16, 20715−20724

Read Online

ACCESS | Metrics & More | Article Recommendations | Supporting Information

ABSTRACT: The core−shell structure is an effective means to improve the stability and optoelectronic properties of cesium lead halide ($CsPbX_3$ (X = Cl, Br, I)) perovskite quantum dots (QDs). However, confined by the ionic radius differences, developing a core−shell packaging strategy suitable for the entire $CsPbX_3$ system remains a challenge. In this study, we introduce an optimized hot-injection method for the epitaxial growth of the $CsPb_2X_5$ substrate on $CsPbX_3$ surfaces, achieved by precisely controlling the reaction time and the ratio of lead halide precursors. The synthesized $CsPbX_3/CsPb_2X_5$ composite microplates exhibit an emission light spectrum that covers the entire visible range. Crystallographic analyses and density functional theory (DFT) calculations reveal a minimal lattice mismatch between the (002) plane of $CsPb_2X_5$ and the $(1\bar{1}0)$ plane of $CsPbX_3$, facilitating the formation of high-quality type-I heterojunctions. Furthermore, introducing Cl^- and I^- significantly alters the surface energy of $CsPb_2X_5$'s (110) plane, leading to an evolutionary morphological shift of grains from circular to square microplates. Benefiting from the passivation of $CsPb_2X_5$, the composites exhibit enhanced optical properties and stability. Subsequently, the white light-emitting diode prepared using the $CsPbX_3/CsPb_2X_5$ composite microplates has a high luminescence efficiency of 136.76 lm/W and the PL intensity decays by only 3.6% after 24 h of continuous operation.

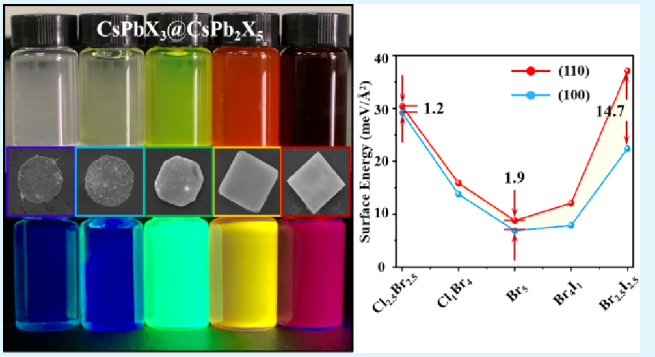

KEYWORDS: *perovskites, quantum dots, composites, $CsPb_2Br_5$, optoelectronic devices*

INTRODUCTION

Cesium halide lead ($CsPbX_3$ (X = Cl, Br, I)) perovskite quantum dots (QDs) have garnered significant interest in the research community due to their tunable bandgap, superior photoluminescence quantum yields (PLQY), and exceptional charge-transfer characteristics.[1−4] However, the commercialization of this family of QDs is impeded by challenges, such as a high density of defect states, a propensity for surface ligand desorption, and significant stability concerns.[5−8] Consequently, extensive research has focused on enhancing the ionic properties of $CsPbX_3$ QDs, employing techniques such as sensitizer doping,[9] heterogeneous shell encapsulation,[10] and strong binding energy ligands anchoring surface.[11,12] Notably, the passivation of QDs through core−shell structuring has emerged as a particularly effective strategy, enhancing both stability and optical performance.[13−15] This technique effectively isolates QDs from external environmental factors by employing stable and heterogeneous shells as protective barriers. Simultaneously, it facilitates the formation of high-quality heterojunctions, thereby inspiring innovative methodologies in perovskite material development.

Currently, various strategies for constructing core−shell structures in $CsPbX_3$ QDs have been developed, primarily encompassing: (i) encapsulation using oxides or other mesoporous materials, including TiO_2,[16−18] SiO_2,[19−21] ZrO_2,[22] and PbBr(OH).[23] These encapsulation processes typically involve the hydrolysis of ester compounds with direct participation of water, while the crystallization and growth of oxide shells also require secondary annealing.[16] Such harsh experimental conditions can lead to the dissolution or thermal decomposition of QDs. Additionally, the products also face problems, such as large size (typically micron or submicron scale), presence of holes on the surface, and impeded charge transfer, resulting in low quantum yields. (ii) Epitaxial growth of heterogeneous shells, including Cs_4PbBr_6,[24] $CsPb_2Br_5$,[14,25] and ZnS.[26] This approach effectively circumvents the aforementioned issues, typically forming nanoscale shells that encapsulate a single QD core or a few QD cores, thereby ensuring complete QD coverage. However, limited by the ionic

Received: January 4, 2024
Revised: March 27, 2024
Accepted: March 28, 2024
Published: April 10, 2024

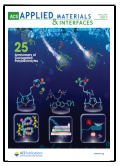

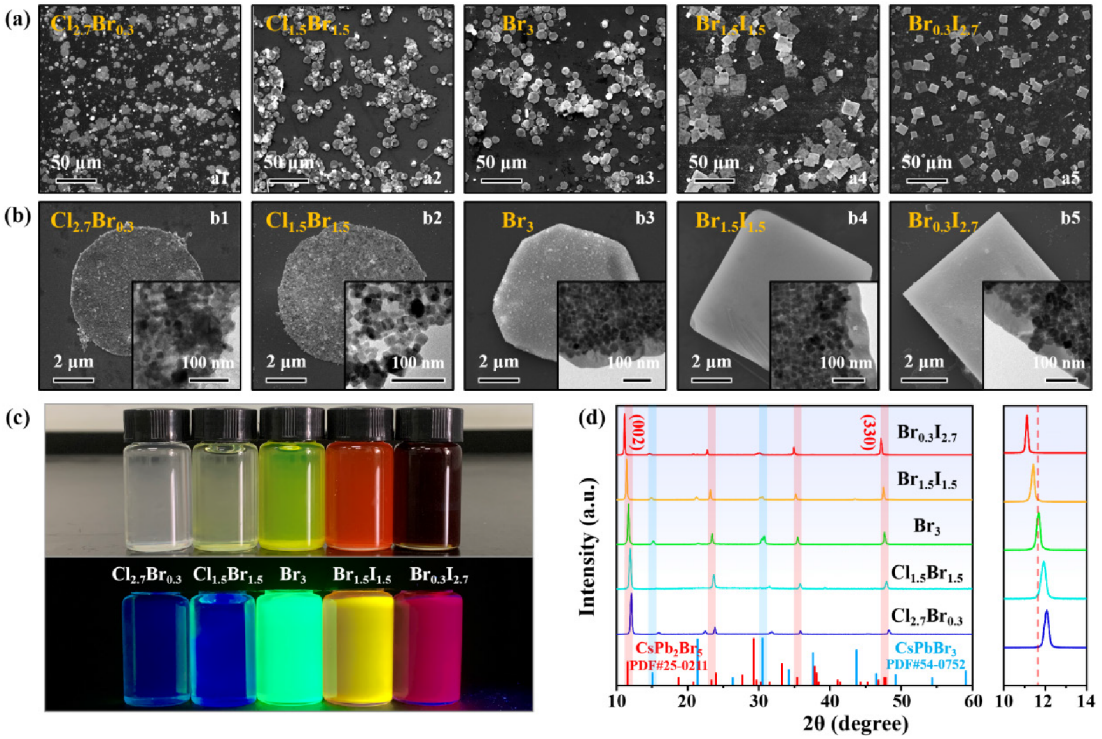

Figure 1. SEM images of (a) the overall morphology and (b) individual grains of $CsPbX_3/CsPb_2X_5$ CMs. The insets show the corresponding TEM images of the samples. (c) Photographs of colloidal solutions of $CsPbX_3/CsPb_2X_5$ CMs under daylight and UV (365 nm) excitation. (d) XRD pattern of $CsPbX_3/CsPb_2X_5$ CMs.

radius difference and crystal structure rigidity, the products often present disadvantages such as nontunable fluorescence emission, complicated synthesis process, and low yield, making some ingenious synthetic ideas unable to be further extended to the entire $CsPbX_3$ perovskite material system. Therefore, there is an urgent need for a universal improvement strategy that can be applied across $CsPbX_3$ QDs with varied halogen elements, while also addressing the materials' instability and enhancing optoelectronic performance.

In this study, we introduce an advanced hot-injection method to epitaxially grow a $CsPb_2X_5$ substrate on $CsPbX_3$ QD surfaces, achieved by a controlled ratio of lead halide precursors and extended reaction times. The obtained $CsPbX_3/CsPb_2X_5$ grains exhibit morphologies transitioning from circular to octagonal to square with the alteration of anions from Cl^- to Br^- to I^-, while their emission spectrum encompasses the entire visible range. Microstructural analysis reveals that the lattice mismatch between the (002) plane of $CsPb_2X_5$ and the $(1\bar{1}0)$ plane of $CsPbX_3$ ranges only from 4.3% to 14.6%, facilitating the epitaxial growth of $CsPb_2X_5$ on the $CsPbX_3$ "seed." Meanwhile, density functional theory (DFT) calculations and thermodynamic analyses demonstrate that the change in the anionic component ($Cl^- \rightarrow Br^- \rightarrow I^-$) significantly increases the surface energy of $CsPb_2X_5$'s (110) plane compared to its (100) plane. This differential leads to a shift in the crystal growth orientation, causing the grains to evolve from circular to square microplates. Benefiting from the $CsPb_2X_5$ substrate, which passivate surface defects and form type-I heterojunctions with the $CsPbX_3$, the composites exhibit enhanced PLQY and remarkable stability. White LEDs prepared using $CsPbX_3/CsPb_2X_5$ composite microplates exhibit surprisingly high luminous efficacy of 136.76 lm/W and sustained operating stability under high temperature environment (>105 °C).

RESULTS AND DISCUSSION

Preparation and Morphology of $CsPbX_3/CsPb_2X_5$ Composite Microplates. In this study, $CsPbX_3/CsPb_2X_5$ composite microplates were obtained in one step by the conventional hot-injection method without an additional post-treatment process. Briefly, 0.3 mmol of lead halide ($PbCl_2$, $PbBr_2$, and PbI_2) was dissolved in the ODE, and then 0.15 mmol of cesium oleate (Cs^+: Pb^{2+} = 1:2) was injected to react for 1 h, inducing epitaxial growth of $CsPb_2X_5$ on the surface of QDs. Moreover, by replacing the lead halide salts in specific ratios, the emitted light of $CsPbX_3/CsPb_2X_5$ composite microplates (denoted as X_3 CMs) could cover the entire visible region. For example, $CsPbCl_{2.7}Br_{0.3}/CsPb_2(Cl/Br)_5$ composite microplates ($Cl_{2.7}Br_{0.3}$ CMs), with $PbCl_2$: $PbBr_2$ = 9:1 in the precursor.

First, the morphology of products was observed by scanning electron microscopy (SEM) (Figure 1a,b). $Cl_{2.7}Br_{0.3}$ CMs are circular microplates (Figure 1a1,b1) with an average size of about 5.07 μm (Figure S1a); the grain shape of $Cl_{1.5}Br_{1.5}$ CMs was essentially unchanged (Figure 1a2, b2), but the size increased slightly to 6.28 μm (Figure S1b). The morphology of pure Br_3 CMs evolved from circular to octagonal microplates (Figure 1a3,b3), and the size further increased to 7.4 μm (Figure S1c). Continuing the introduction of I^-, the grains of $Br_{1.5}I_{1.5}$ CMs evolved from octagonal to square microplates (Figure 1a4, b4) and the size increased to 9.72 μm (Figure S 1d); when I^-: Br^- was raised to 9:1, the corners of $Br_{0.3}I_{2.7}$ CMs became more sharper (Figure 1a5, b5) but the grain size decreased to 7.69 μm (Figure S1e). We considered that the difference in ionic radius was the primary factor leading to the

https://doi.org/10.1021/acsami.4c00178
ACS Appl. Mater. Interfaces 2024, 16, 20715−20724

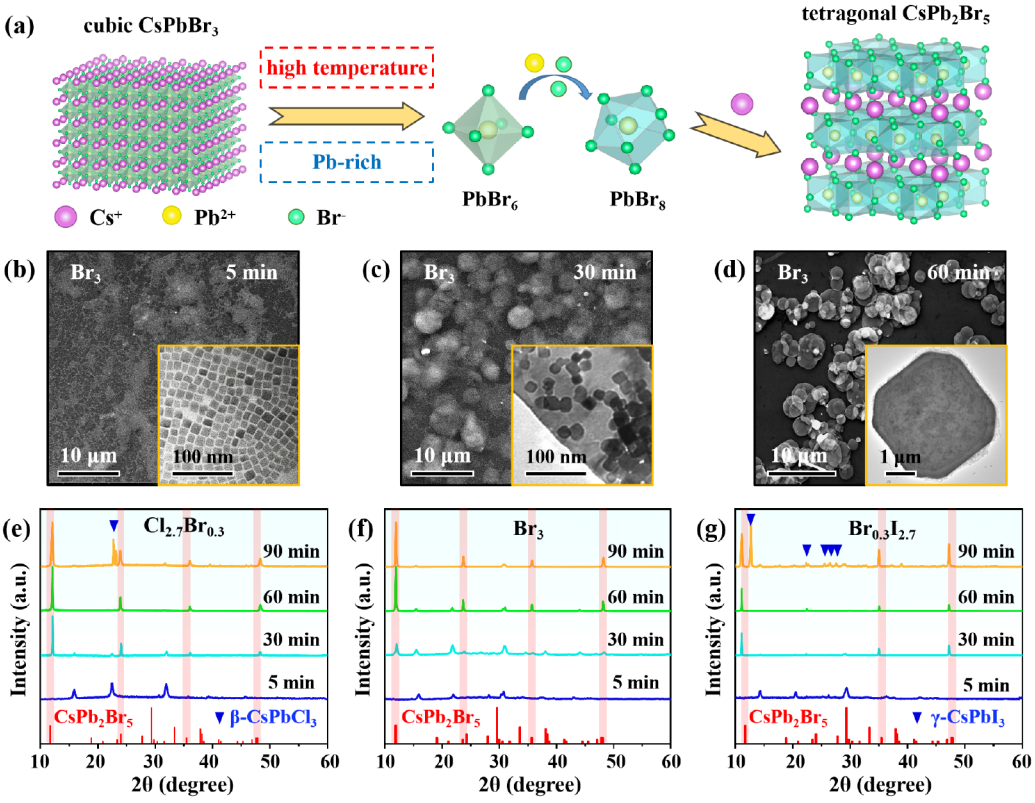

Figure 2. (a) Schematic representation of the transformation of cubic $CsPbBr_3$ into tetragonal $CsPb_2Br_5$. SEM and TEM images of Br_3 CMs after (b) 5 min, (c) 30 min, and (d) 60 min reactions. XRD patterns of (e) $Cl_{2.7}Br_{0.3}$ CMs, (f) Br_3 CMs, and (g) $Br_{0.3}I_{2.7}$ CMs after 5, 30, 60, and 90 min reactions.

variation in grain size. As the anionic component follows the trend from Cl^- to Br^- to I^-, the ionic radius gradually increases, resulting in lattice expansion, and the grain size increases. However, the excess I^- in $Br_{0.3}I_{2.7}$ CMs (i.e., lack of Br^- in the reaction) prevented the $CsPb_2X_5$ substrate from growing sufficiently, and therefore, the grain size was reduced. Subsequently, transmission electron microscope (TEM) images observed a large number of monodisperse cubic $CsPbX_3$ QDs inside the microplate (Figure 1b1−5); moreover, the energy dispersive spectra (EDS) showed that all elements were uniformly distributed in the microplates and the Cs: Pb: Cl/Br/I of the samples were in the range of 1:1:3 to 1:2:5, which preliminary indicated that $CsPbX_3$ were embedded inside $CsPb_2X_5$ (Figure S2 and Table S1).

Further, Figure 1c shows photographs of the samples under daylight and UV light (365 nm), and it could be found that $CsPb_2X_5$ could selectively allow Cl^- and I^- to penetrate into the shell layer, enabling convenient control of the luminescence of the materials by adjusting the anionic component. The X-ray diffraction (XRD) spectra indicated the presence of two different characteristic peaks in the composites, corresponding to $CsPbX_3$ QDs and the $CsPb_2X_5$ substrate (Figure 1d), and the sharp diffraction peaks of $CsPb_2X_5$ proved that the materials had excellent crystallinity. It was worth noting that all the diffraction peaks of $CsPbX_3$ and $CsPb_2X_5$ were shifted to large angles with increasing Cl^-, and shifted to small angles with increasing I^-. This lattice shrinkage/expansion demonstrated that Cl^- and I^- were present not only in $CsPbX_3$ but also in the $CsPb_2X_5$ substrate. Overall, the SEM and XRD results proved that highly uniform $CsPbX_3/CsPb_2X_5$ composite microplates could be obtained in one step by controlling the ratio of precursors and the reaction time.

The above results indicated that the ratio of lead halide and reaction time were the key factors in inducing formation of the $CsPb_2X_5$ substrate. In order to reveal the growth process of $CsPb_2X_5$, we first investigated the samples at different reaction times using Br_3 CMs as an example. The previous studies have shown that, since the nucleation and crystallization of $CsPbX_3$ QDs rapidly followed thermodynamic processes, the preparation of QDs by hot-injection method would require immediate quenching within 5−10 s after Cs-OA injection to inhibit nanocrystal growth and unwanted product formation.[27] On prolonging the reaction time, the generated $[PbBr_3]^-$ complex would continue to react with Pb^{2+} and Br^- to obtain the $[Pb_2Br_5]^-$ complex due to high temperature, Pb-rich and Br-rich environments, i.e., the $PbBr_6$ octahedron was broken and embedded with additional Pb^{2+} and Br^- ions to form the $PbBr_8$ undecahedron (Figure 2a). Subsequently, the $PbBr_8$ polyhedra shared Br atoms at top corners, forming the tetragonal $[Pb_2Br_5]^-$ layer, and combined with Cs^+ in solution to compose the basic cell of $CsPb_2Br_5$. This process can be summarized in the following two steps:

$$[PbBr_3]^- + PbBr_2 \rightarrow [Pb_2Br_5]^- \quad (1)$$

$$[Pb_2Br_5]^- + Cs^+ \rightarrow CsPb_2Br_5 \quad (2)$$

Unlike rapidly crystallizing $CsPbX_3$, the formation of $CsPb_2Br_5$ was much slower, which was more conducive to precise control of the reaction products. Subsequently, SEM and TEM exhibited the morphology of the samples at different reaction times. In the first 5 min of reaction, the products were

https://doi.org/10.1021/acsami.4c00178
ACS Appl. Mater. Interfaces 2024, 16, 20715−20724

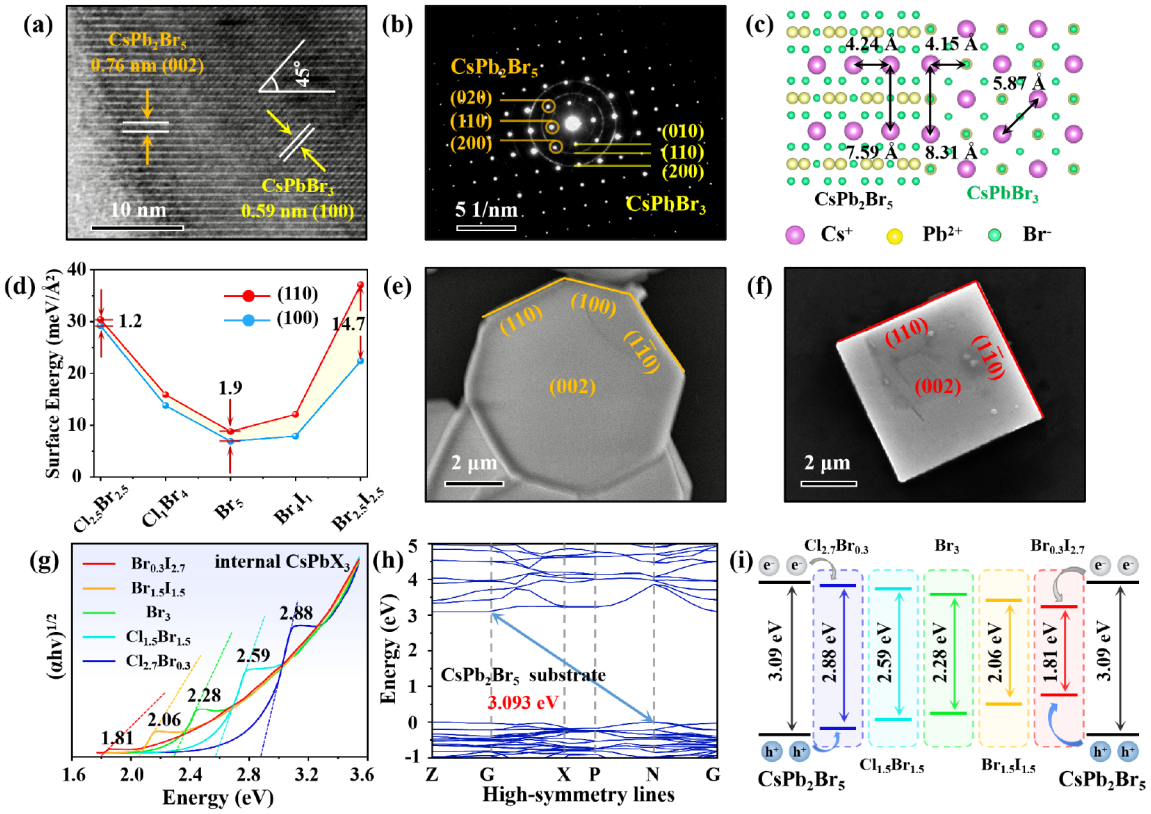

Figure 3. (a) HRTEM image of $CsPbX_3/CsPb_2X_5$ CMs prepared by controlling Cs^+: Pb^{2+} to 1:2 in the precursor and reacting for 1 h. (b) SAED image of $CsPbX_3/CsPb_2X_5$ CMs. (c) Atomic modeling of the $CsPbBr_3$−$CsPb_2Br_5$ heterojunction. (d) Surface energy of the (110) and (100) planes of $CsPb_2X_5$. Schematic of the lattice plane distribution of (e) Br_3 CMs and (f) $Br_{0.3}I_{2.7}$ CMs. (g) Optical band gap of $CsPbX_3$ QDs cores. (h) The electronic structures of tetragonal $CsPb_2Br_5$. (i) Energy band diagrams of the $CsPbX_3/CsPb_2X_5$ CMs.

uniform cubic $CsPbBr_3$ QDs, and no other phases were observed (Figure 2b). When the reaction proceeded to 30 min, all QDs were no longer uniformly dispersed on silicon wafers but reorganized into circular microcrystals (Figure 2c). At this point, TEM observed that QDs were embedded inside other 2D film-like materials (Figure 2c inset). The characteristics of this new phase were consistent with $CsPb_2Br_5$, which was usually reported as 2D film-like materials because of the lamellar crystal structure of $CsPb_2Br_5$.[28,29] When the reaction proceeded for 60 min, the grains further grew into regular octagonal microplates, marking the completion of the growth of the $CsPbX_3/CsPb_2X_5$ composite structure (Figure 2d).

The XRD results showed that when the reaction proceeded to 30 min, a new diffraction peak corresponding to the (002) plane of $CsPb_2Br_5$ at 11.9° appeared in Br_3 CMs, but the lower peak intensity indicated that $CsPb_2Br_5$ had low crystallinity and could not yet form dense shell layers (Figure 2f). Further, the reaction time was extended to 60 min; the diffraction peak at 11.9° was sharper, and $CsPb_2Br_5$ continued to grow at that stage, resulting in the complete encapsulation of $CsPbBr_3$ QDs. Finally, when the reaction reached 90 min, the diffraction peaks of $CsPbBr_3$ QDs decreased significantly, and the composites gradually evolved into pure $CsPb_2Br_5$. As for $Cl_{2.7}Br_{0.3}$ CMs (Figure 2e) and $Br_{0.3}I_{2.7}$ CMs (Figure 2g), besides XRD peak position shifting due to differences in ionic radii, both experienced a growth process similar to that of Br_3 CMs in the first 60 min, corresponding to the nucleation and growth of the $CsPb_2X_5$ substrate. But differently, at 90 min for $Cl_{2.7}Br_{0.3}$ CMs, the diffraction peak at 22.8° was attributed to the tetragonal $CsPbCl_3$ (β-$CsPbCl_3$, PDF#18−0366) with lower symmetry;[31] at 90 min for $Br_{0.3}I_{2.7}$ CMs, the diffraction peak of the orthorhombic $CsPbI_3$ (γ-$CsPbI_3$, PDF#18−0376) appeared.[30,32] Therefore, precise control of the reaction time could avoid the generation of impurity phases and enable the stabilized $CsPb_2X_5$ to tightly package the internal $CsPbX_3$ QDs.

Heterojunction and DFT Calculations. In addition to the reaction time, another important parameter addressed in this paper was the ratio of PbX_2 in precursor, since the excess of lead halide was beneficial in inducing the formation of $CsPb_2X_5$.[33,34] In order to understand the effect of this condition, the morphology and crystal structure of the samples were first investigated when Cs^+: Pb^{2+} = 1:1. The results are shown in Figure S3a; even if the reaction time was extended to 1 h, the samples prepared with a low proportion of lead halides were still typical cubic phase $CsPbBr_3$ nanocrystals, which were insufficient to form the $CsPb_2Br_5$ substrate. The corresponding HRTEM result indicated that the 0.59 nm spacing was assigned to the (100) and (010) planes of $CsPbBr_3$, and 0.41 nm was assigned to the (110) plane (Figure S3b). Subsequently, after increasing Cs^+: Pb^{2+} to 1:2 and keeping the same reaction time, HRTEM observed two distinct lattice fringes (Figure 3a), corresponding to the (002) plane (0.76 nm) of tetragonal $CsPb_2Br_5$ and the (100) plane (0.59 nm) of cubic $CsPbBr_3$, demonstrating that a high proportion (1:2) of the lead halide promoted the formation of $CsPb_2Br_5$. According to the thermodynamics of crystal growth, in order to make the $CsPbBr_3$ and $CsPb_2Br_5$ composites have the lowest overall energy, the lattice of $CsPbX_3$ was rotated by 45° to ensure that the heterojunction had the smallest lattice

https://doi.org/10.1021/acsami.4c00178
ACS Appl. Mater. Interfaces 2024, 16, 20715−20724

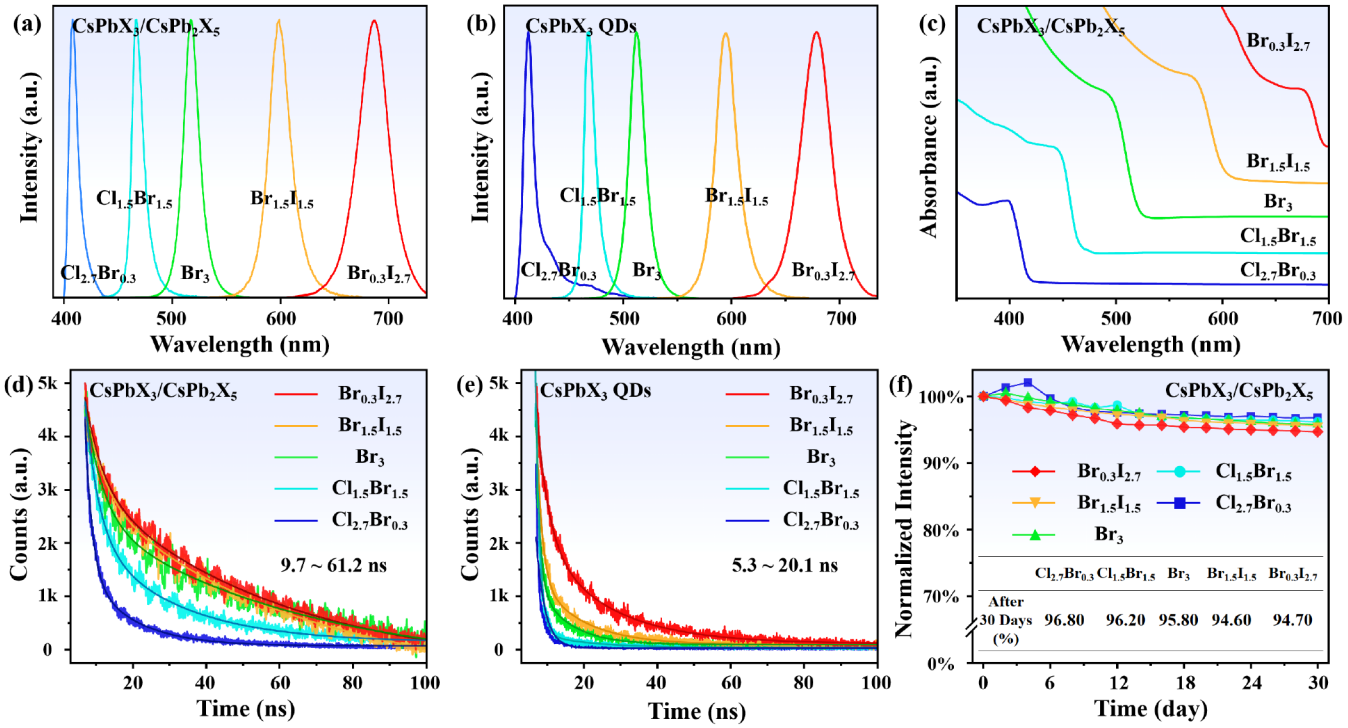

Figure 4. PL spectra of (a) $CsPbX_3/CsPb_2X_5$ CMs and (b) $CsPbX_3$ QDs (λ = 365 nm). (c) UV−vis absorption spectra of $CsPbX_3/CsPb_2X_5$ CMs. Time-resolved fluorescence spectra of (d) $CsPbX_3/CsPb_2X_5$ CMs and (e) $CsPbX_3$ QDs. (f) Water stability test results for $CsPbX_3/CsPb_2X_5$ CMs.

mismatch. Selected-area electron diffraction (SAED) indicated that the $CsPb_2Br_5$ substrate was the typical single-crystal diffraction point and the internal $CsPbBr_3$ QDs were polycrystalline ring stripes (Figure 3b). The overall structure of the composites was a large number of nanoscale QDs (10−20 nm) embedded in micrometer-scale $CsPb_2Br_5$ (5−10 μm) single crystals. This embedded structure effectively avoided the large number of grain boundaries present in tiny composites leading to the high density of defect states during the epitaxial growth of nanoscale shells. Meanwhile, the long-range ordered $CsPb_2X_5$ single crystal would be able to fill the halogen vacancies on the surface of QDs and reduce the nonradiative recombination paths. Based on the above results, the atomic model of the $CsPbX_3$-$CsPb_2Br_5$ heterojunction is shown in Figures 3c and S4. For the $CsPbCl_3$−$CsPb_2Br_5$ heterojunction, along the *c*-axis direction, the (002) plane (d = 7.59 Å) of $CsPb_2Br_5$ and the (1$\bar{1}$0) plane (d = 7.93 Å) of $CsPbCl_3$ were matched with lattice mismatch of <4.3% (Figure S4a). Along the *a*-axis direction, the (200) plane (d = 4.24 Å) of $CsPb_2Br_5$ and the (110) plane (d = 3.96 Å) of $CsPbCl_3$ were matched with lattice mismatches <6.6%. Similarly, the lattice mismatch was about 8.6% (*c*-axis direction) and 3.2% (*a*-axis direction) for the $CsPbBr_3$−$CsPb_2Br_5$ heterojunction (Figure 3c); the lattice mismatch was about 14.6% (*c*-axis direction) and 4.9% (*a*-axis direction) for the $CsPbI_3$−$CsPb_2Br_5$ heterojunction (Figure S4b). This slight lattice mismatch would ensure the smooth epitaxial growth of $CsPb_2Br_5$ on the surface of $CsPbX_3$, allowing the QDs to act as "seeds" for the formation of $CsPbX_3/CsPb_2X_5$ composite materials.

Since grains with different morphologies tend to expose different crystal planes and the surface atomic densities and electronic structures of the individual crystal planes lead to materials exhibiting distinct physical and chemical properties, it would be instructive to reveal the reasons for the evolution of the composites from circular to octagonal to square. Previous XRD results showed that the (002) plane (at 11.9°) of $CsPbX_3/CsPb_2X_5$ CMs had the highest diffraction intensity, but with the change of anions, the peak intensity of the (330) plane gradually increased, and the ratio of two peaks ($I_{(002)}/I_{(330)}$) decreased from 8.93 to 2.49 (Figure 1d). This phenomenon inspired us to consider that the evolution of CMs from circular to square might be caused by the change in the lateral growth rate. Subsequently, the surface energies of (110) and (100) crystal planes were calculated by density-functional theory (DFT), in order to identify the specific growth directions of $CsPbX_3/CsPb_2X_5$ CMs. The calculation of the surface energy E_{surf} followed the below equation:

$$E_{surf} = \frac{E_{Slab} - nE_{Bulk}}{2A} \quad (3)$$

where E_{Slab} was the model slab energy; n was the atomic number ratio; E_{Bulk} was the total energy of the cell; and A was the cross-sectional area of the crystal surface. The ratios of Cl/Br and I/Br were limited to 0−1 to avoid the crystal structure of $CsPb_2X_5$ being altered by excessive anion exchange. The detailed computational model and parameters are shown in Figure S5 and Table S2.

The results indicated (Figure 3d) that both $E_{(110)}$ and $E_{(100)}$ increased with increasing Cl^- or I^- doping, and the (110) plane had the higher surface energy compared to the (100) plane. However, the difference was a significant change in $E_{(110)}/E_{(100)}$, which increased from 1.04 ($CsPb_2Cl_{2.5}Br_{2.5}$) to 1.27 ($CsPb_2Br_5$) and to 1.66 ($CsPb_2Br_{2.5}I_{2.5}$). According to the symmetry of the $CsPb_2Br_5$ crystal structure, the top and bottom planes of the microplates were attributed to the (002) plane of $CsPb_2Br_5$, while the higher surface energy of the lateral (110) plane implied that the grains would prefer to grow along the direction normal to this plane ([110]

https://doi.org/10.1021/acsami.4c00178
ACS Appl. Mater. Interfaces 2024, 16, 20715−20724

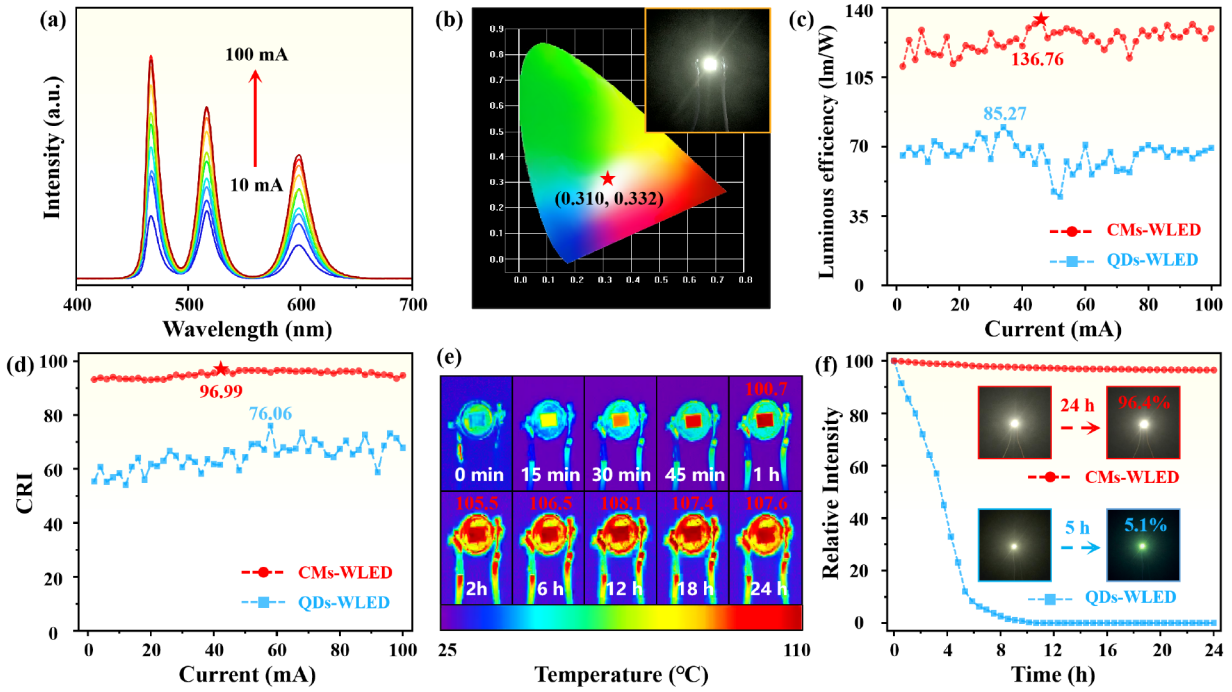

Figure 5. (a) PL spectra of CMs-WLED at 10−100 mA drive current. (b) CIE coordinates of CMs-WLED at 40 mA drive current, and the inset showed EL photograph of CMs-WLED. Comparison of (c) luminous efficiency and (d) CRI of CMs-WLED at 2−100 mA driving current. Comparison of (e) surface temperature and (f) stability of CMs-WLED operating continuously for 24 h at a 40 mA driving current.

direction).[31,35] In $CsPb_2Cl_{2.5}Br_{2.5}$, $E_{(110)}/E_{(100)} \approx 1$ represented the same growth rate in the [100] and [110] directions, and it was predicted that the resulting grains should be regular octagonal plate grains surrounded by two top or bottom (002) planes, four equivalent {100} planes, and four equivalent {110} planes. However, in order to minimize the total energy, the increased reaction time caused the high-energy angular positions of the octagon to be dissolved and the microplates transformed into circular shapes (corresponding to $Cl_{2.7}Br_{0.3}$ CMs). For $CsPb_2Br_5$, $E_{(110)}/E_{(100)}$ = 1.27, resulting in an irregular octagon surrounded by two (002) planes, four short {100} planes, and four long {110} planes (corresponding to Br_3 CMs) (Figure 3e). This transformation of the octagon into the circle was demanding because it required much higher external energies to dissolve sharper edges and corners. For $CsPb_2Br_{2.5}I_{2.5}$, $E_{(100)}$ is much smaller than $E_{(110)}$, and the grains grew preferentially in the *ab*-plane along the [110] direction, where the (100) plane was masked by the fast-growing (110) plane, which evolved into the square surrounded by two (002) planes and four equivalent {110} planes (corresponding to $Br_{0.3}I_{2.7}$ CMs) (Figure 3f). Thus, the difference in surface energy between the (100) and (110) plane was the fundamental reason for the change of grains from circular to octagonal to square. Finally, based on the absorption spectra (Figure 3g) and DFT calculations (Figure 3h), we obtained the band gaps of $CsPbX_3$ cores and $CsPb_2X_5$, and aligned the energy bands of both according to previous reports.[36,37] The results showed (Figure 3i) that a typical type-I heterojunction was formed between the two, and this structure allowed carriers to be limited in the energy bands of $CsPbX_3$ QDs for recombination, which enhanced the photoemission.[38]

Optical Properties of $CsPbX_3/CsPb_2X_5$ Composite Microplates. Further, we investigated the optical properties of $CsPbX_3/CsPb_2X_5$ CMs. First, the PL spectra shown in Figure 4a indicated that the emission light of CMs could cover the entire visible region (410−687 nm) by replacing different halogen elements. This range was wider than the same ratio of $CsPbX_3$ QDs (415−679 nm) (Figure 4b and Table S3), attributable to the non-PL active $CsPb_2X_5$ substrate consuming most of Br^- in the system, and thus the peak positions were closer to the pure $CsPbCl_3$ (~406 nm) and $CsPbI_3$ QDs (~690 nm). Meanwhile, the emission peaks of $CsPbX_3/CsPb_2X_5$ CMs exhibited more symmetrical shapes and narrower full width at half-maximum (fwhm). Especially for PLQY, CMs had the high quantum yield of 76%−91%, while QDs were only 32%−59%, improving about 1.5−2.4 times (Table S3). Subsequently, the ultraviolet−visible (UV−vis) absorption spectra of the composites exhibited sharp exciton absorption peaks of $CsPbX_3$ QDs, further demonstrating that the $CsPb_2X_5$ substrate would not affect the inherent optical properties of the internal QDs (Figure 4c). In order to visually demonstrate the light enhancement effect of $CsPb_2X_5$, we compared the PL decay lifetimes of $CsPbX_3/CsPb_2X_5$ CMs and $CsPbX_3$ QDs. The results showed that the average lifetimes of the CMs were 10.7−61.2 ns (Figure 4d), whereas the QDs were only 5.3−20.1 ns (Figure 4e), extending about 2−4 times (Table S3). The first reason for PLQY and fluorescence lifetimes being greatly improved was the decreased density of defect states in the QD cores. $CsPb_2X_5$ could effectively fill the dangling bonds on the surface of QDs and limit the doping of Pb atoms to improve the radiative recombination rate. The second reason was that this embedded structure allowed QDs to be uniformly dispersed in the $CsPb_2X_5$ substrate, preventing self-absorption/reabsorption effects caused by aggregation.[39] The third reason was attributed to the broad-band $CsPb_2X_5$ forming the quantum well structure with the narrow-band $CsPbX_3$, which improved the quantum efficiency of the composites.

Finally, we tested the stability of the composites in different environments. First, the water stability results showed that for

https://doi.org/10.1021/acsami.4c00178
ACS Appl. Mater. Interfaces 2024, 16, 20715−20724

bare $CsPbX_3$ QDs, the PL intensity decreased dramatically and the peak position was significantly shifted due to the decomposition of crystal structure after 3 h of immersion (Figure S6b). In contrast, $CsPbX_3/CsPb_2X_5$ CMs retained more than 94% of the initial PL intensity after 30 days of immersion, with just a 3.2%−5.4% degradation (Figures 4f and S6a). The surprising water stability was mainly attributed to the following reasons: (i) the high decomposition enthalpy of $CsPb_2X_5$ in aqueous environments enabled it to maintain the stable crystal structure for long periods of time.[23] (ii) The surface-adhered $CsPbX_3$ QDs would also be able to react with water to recrystallize into $CsPb_2X_5$,[14] further enhancing the protection of internal QDs. Moreover, benefiting from the protection of $CsPb_2X_5$, the thermal and photo stability of the samples were also greatly improved (Figures S7 and S8). The above results demonstrated that the $CsPb_2X_5$ substrate could effectively reduce the defect state density of QDs and has excellent stability, providing the foundation for applications in fields such as display and illumination.

Through the analysis of microscopic morphology, energy band structure, and optical properties, $CsPbX_3/CsPb_2X_5$ CMs were demonstrated to have the advantages of good dispersion, high luminous efficacy, and high stability. Subsequently, we further explored the application of this material in white light-emitting diode (WLED) devices. We prepared a quasi-perovskite WLED (denoted as CMs-WLED) by selecting $Br_{1.5}Cl_{1.5}$, Br_3, and $Br_{1.5}I_{1.5}$ CMs as the blue, green, and red light sources, encapsulating the materials into polymer films (polystyrene), and integrating on 365 nm UV chips. For comparison, $CsPbX_3$ QDs WLED without $CsPb_2X_5$ passingivation, denoted as QDs-WLED, were prepared using the same strategy.

First, Figure 5a shows the PL spectra of CMs-WLED. Even at a large driving current (100 mA), the shape and position of the emission peaks were not significantly shifted, which initially indicated that the device possessed good luminescence stability. Further, the CIE coordinates of CMs-WLED were stabilized at (0.310, 0.332) with pure white light emission at 40 mA driving current (Figure 5b). Moreover, the device exhibited the highest luminescence efficiency (~136.76 lm/W) at a 46 mA drive current, which exceeded QDs-WLED by 61.6% (~85.27 lm/W) (Figure 5c). Meanwhile, CMs-WLED also had a higher and stable color rendering index (CRI), which exceeded 90 under all current conditions (maximum 96.99), while QDs-WLED were only 76 at the highest (Figure 5d). The narrower fwhm was considered to be the main reason for the higher color rendering index. CMs had fwhm of 10−31 nm, while QDs had fwhm of 12−37 nm (Table S2), allowing CMs to excite purer light and therefore had better displays.[40] Finally, the high temperature generated during the operation of optoelectronic devices was one of the key factors deteriorating the luminescence of perovskite materials.[41] We recorded the surface temperature of CMs-WLED by an infrared imager, which proved that the composites had the same long-term stability even under harsh working conditions. As the results shown in Figure 5e, the center temperature of LED substrate had exceeded 100 °C after 1 h of continuous operation and remained at 105−110 °C for the following 2−24 h. However, CMs-WLED showed surprising stability, with the PL intensity decaying by only 3.6% even after 24 h of continuous operation (Figure 5f). In sharp contrast, QDs-WLED decayed to 5.1% of luminous intensity after 6 h of operation, and the device no longer had its original white light emission due to the thermal decomposition of QDs. These performances exhibited significant advantages compared to previous reports (Table S4). Above all, the advantages of $CsPbX_3/CsPb_2X_5$ composites, such as higher luminescence efficiency and more stable working performance, would greatly expand the applications of perovskite materials in the field of optoelectronics.

CONCLUSION

In summary, a series of homogeneous $CsPbX_3/CsPb_2X_5$ composite microplates were prepared by controlling the reaction time and the ratio of the lead halide precursors. The resulting composites had circular, octagonal, and square morphology and the excitation light covered the entire visible region. Subsequently, observations of the heterojunction microstructure and DFT calculations indicated that the lattice of $CsPbX_3$ was distorted by 45° to achieve minimal lattice mismatch, and the change in crystal growth orientation caused by the surface energy difference between the (110) and (100) planes was the determining factor in morphological evolution. Benefiting from the stable crystal structure of the $CsPb_2X_5$ substrate, effective passivation of surface defects, and high-quality type-I heterojunction, the quantum yield and stability of the $CsPbX_3$ QDs were significantly improved. The quasi-white LEDs prepared using the composites had a high luminous efficiency of 136.76 lm/W and a color rendering index of 96.99, and the EL intensity was essentially unchanged after operating for 24 h in a harsh environment above 105 °C. This innovative strategy paves the way for advancing a broader perovskite material system using composite structures.

EXPERIMENTAL SECTION

Materials. Cesium carbonate (Cs_2CO_3, 99.99%), lead(II) chloride ($PbCl_2$, 99.99%), lead(II) bromide ($PbBr_2$, 99.99%), lead(II) iodide (PbI_2, 99.99%), oleic acid (OA, 85%), oleylamine (OAm, 80−90%), 1-octadecene (ODE, 90%), and toluene (>99.7%) were purchased from Aladdin. Poly(styrene) (PS) was purchased from Macklin. 365 nm blue light chips (5 W) were purchased from CREE company. All the reagents were used without further purification.

Synthesis of $CsPbX_3/CsPb_2X_5$ Composite Microplates (X_3 CMs). 2.5 mmol of Cs_2CO_3 was placed in a solution consisting of 2.5 mL of OA and 10 mL of ODE and transferred to a 100 mL three-neck flask. The solution was heated to 120 °C under vacuum and reacted for 1 h. After that, the Cs-OA precursor was obtained by heating to 140 °C and reacting for 1 h under a N_2 environment. Note that the Cs-OA precursor needs to be held at 100 °C before use.

0.3 mmol PbX_2 (e.g., $Cl_{2.7}Br_{0.3}$ CMs, 0.027 mmol $PbCl_2$ and 0.03 mmol $PbBr_2$) was placed in a solution consisting of 10 mL ODE, 0.5 mL OA, and 0.5 mL OAm and transferred to another 100 mL three-neck flask. The temperature was increased to 120 °C under N_2 and held for 1 h. After that, the temperature was again increased to 170 °C for 10 min and 0.3 mL of Cs-OA was injected into the solution. After 60 min of reaction, the three-neck flask was immersed in ice−water to terminate the reaction. The precipitates were obtained by centrifugation of the crude solution at 1000 rpm/min for 5 min and washed 2−3 times with toluene. Finally, the precipitation was dispersed into 15 mL toluene to obtain $CsPbX_3/CsPb_2X_5$ composite microplates solution.

Preparation of White Light-Emitting Diodes (CMs-WLED). 15 mL $CsPbX_3/CsPb_2X_5$ CMs toluene solution and 0.5 g PS particles were stirred at 60 °C for 3 h. Then, the solution was poured into prefabricated molds, and $CsPbX_3/CsPb_2X_5$ polymer films were deposited at room temperature. Finally, three films of $Cl_{1.5}Br_{1.5}$, Br_3 and $Br_{1.5}I_{1.5}$ were covered on a 365 nm blue light chip to obtain CMs-WLED.

Characterization. The microstructure and EDS spectra of samples were analyzed by HRTEM (JEOL JEM-F200) with an

https://doi.org/10.1021/acsami.4c00178
ACS Appl. Mater. Interfaces 2024, 16, 20715−20724

energy-dispersive spectrometer (EDS). The morphology of the samples were investigated by field-emission scanning electron microscopy (FESEM, FEI Quatan FEG 250). Photoluminescence (PL) spectra and time-resolved PL (TRPL) decay curves of samples were recorded on an Edinburgh Instruments FLS1000 spectrometer. The ultraviolet−visible (UV−vis) absorption spectra were recorded with a Jasco V-570 UV/vis/NIR spectrophotometer. X-ray diffraction (XRD) patterns of samples were obtained with a DB-ADVANCE X-ray diffractometer. The electroluminescence (EL) spectra, luminous efficiency, color rendering index (CRI) and chromaticity coordinate of WLED were obtained with a Keithley 2400 light meter and Photo Research 670 spectrometer. The CMs-WLED surface temperature was detected and recorded using a thermal infrared imager (FOTRIC, USA).

■ ASSOCIATED CONTENT

Supporting Information

The Supporting Information is available free of charge at https://pubs.acs.org/doi/10.1021/acsami.4c00178.

The size distribution of the samples; EDS spectra of the samples; computational model of $CsPb_2X_5$; optical band gap of $CsPbX_3$ QDs cores; the electronic structures of tetragonal $CsPb_2Br_5$; PL spectra and time-resolved fluorescence spectra of $CsPbX_3$ QDs; comparison of water stability of CMs and QDs (PDF)

■ AUTHOR INFORMATION

Corresponding Authors

Zeyu Wang − *Frontier Institute of Science and Technology (FIST), Xi'an Jiaotong University, Xi'an, Shaanxi 710049, China*; Email: zeyu.wang@xjtu.edu.cn

Minqiang Wang − *Electronic Materials Research Laboratory, Key Laboratory of the Ministry of Education International Center for Dielectric Research & Shannxi Engineering Research Center of Advanced Energy Materials and Devices, Xi'an Jiaotong University, Xi'an 710049, China*; Email: mqwang@mail.xjtu.edu.cn

Authors

Chen Zhang − *Electronic Materials Research Laboratory, Key Laboratory of the Ministry of Education International Center for Dielectric Research & Shannxi Engineering Research Center of Advanced Energy Materials and Devices, Xi'an Jiaotong University, Xi'an 710049, China*; orcid.org/0009-0006-2744-2513

Zheyuan Da − *Electronic Materials Research Laboratory, Key Laboratory of the Ministry of Education International Center for Dielectric Research & Shannxi Engineering Research Center of Advanced Energy Materials and Devices, Xi'an Jiaotong University, Xi'an 710049, China*

Jindou Shi − *Electronic Materials Research Laboratory, Key Laboratory of the Ministry of Education International Center for Dielectric Research & Shannxi Engineering Research Center of Advanced Energy Materials and Devices, Xi'an Jiaotong University, Xi'an 710049, China*; orcid.org/0000-0003-1082-5009

Junnan Wang − *Electronic Materials Research Laboratory, Key Laboratory of the Ministry of Education International Center for Dielectric Research & Shannxi Engineering Research Center of Advanced Energy Materials and Devices, Xi'an Jiaotong University, Xi'an 710049, China*; orcid.org/0000-0002-3074-0195

Youlong Xu − *Electronic Materials Research Laboratory, Key Laboratory of the Ministry of Education International Center for Dielectric Research & Shannxi Engineering Research Center of Advanced Energy Materials and Devices, Xi'an Jiaotong University, Xi'an 710049, China*; orcid.org/0009-0003-0742-8480

Nikolai V. Gaponenko − *Belarusian State University of Informatics and Radioelectronics, Minsk 220013, Belarus*

Arshad Saleem Bhatti − *Centre for Micro and Nano Devices, Department of Physics, COMSATS Institute of Information Technology, Islamabad 44500, Pakistan; Virtual University of Pakistan, Islamabad 44000, Pakistan*

Complete contact information is available at: https://pubs.acs.org/10.1021/acsami.4c00178

Notes

The authors declare no competing financial interest.

■ ACKNOWLEDGMENTS

This work was supported by the National Natural Science Foundation of China (NSFC, 52161145103 and 61774124), National Key R&D Program of China (2022YFE0122500 and 2019YFB1503200), 111 Program (No. B14040), and Shaanxi Provincial Key Research and Development Program (No. 2021GXLH-Z-084). The authors thank Ms Dan He at Instrument Anaysis Center of Xi'an Jiaotong University for her help with the time-resolved PL analysis.

■ REFERENCES

(1) Protesescu, L.; Yakunin, S.; Bodnarchuk, M. I.; Krieg, F.; Caputo, R.; Hendon, C. H.; Yang, R. X.; Walsh, A.; Kovalenko, M. V. Nanocrystals of Cesium Lead Halide Perovskites ($CsPbX_3$, X = Cl, Br, and I): Novel Optoelectronic Materials Showing Bright Emission with Wide Color Gamut. *Nano Lett.* **2015**, *15* (6), 3692−3696.

(2) Lin, K.; Xing, J.; Quan, L. N.; de Arquer, F. P. G.; Gong, X.; Lu, J.; Xie, L.; Zhao, W.; Zhang, D.; Yan, C.; Li, W.; Liu, X.; Lu, Y.; Kirman, J.; Sargent, E. H.; Xiong, Q.; Wei, Z. Perovskite light-emitting diodes with external quantum efficiency exceeding 20%. *Nature* **2018**, *562* (7726), 245−248.

(3) Zhang, A.; Dong, C.; Ren, J. Tuning Blinking Behavior of Highly Luminescent Cesium Lead Halide Nanocrystals through Varying Halide Composition. *J. Phys. Chem. C* **2017**, *121* (24), 13314−13323.

(4) Song, J.; Li, J.; Li, X.; Xu, L.; Dong, Y.; Zeng, H. Quantum Dot Light-Emitting Diodes Based on Inorganic Perovskite Cesium Lead Halides ($CsPbX_3$). *Adv. Mater.* **2015**, *27* (44), 7162−7167.

(5) Zhang, X.; Xu, B.; Zhang, J.; Gao, Y.; Zheng, Y.; Wang, K.; Sun, X. W. All-Inorganic Perovskite Nanocrystals for High-Efficiency Light Emitting Diodes: Dual-Phase $CsPbBr_3$-$CsPb_2Br_5$ Composites. *Adv. Funct. Mater.* **2016**, *26* (25), 4595−4600.

(6) Zhang, C.; Chen, J.; Turyanska, L.; Wang, J.; Wang, W.; Wang, L.; Kong, L.; Wu, K.; Yao, J.; Yao, H.; Yang, Z.; Li, W.; Bekenstein, Y.; Wang, Y.; Jia, G.; Yang, X. Highly Controlled Zigzag Perovskite Nanocrystals Enabled by Dipole-Induced Self-Assembly of Nanocubes for Low-Threshold Amplified Spontaneous Emission and Lasing. *Adv. Funct. Mater.* **2022**, *33*, 2211466.

(7) Wang, K. H.; Wu, L.; Li, L.; Yao, H. B.; Qian, H. S.; Yu, S. H. Large-Scale Synthesis of Highly Luminescent Perovskite-Related $CsPb_2Br_5$ Nanoplatelets and Their Fast Anion Exchange. *Angew. Chem., Int. Ed. Engl.* **2016**, *55* (29), 8328−8332.

(8) Guo, J.; Lu, M.; Zhang, X.; Sun, S.; Han, C.; Zhang, Y.; Yang, X.; Kershaw, S. V.; Zheng, W.; Rogach, A. L. Highly Stable and Efficient Light-Emitting Diodes Based on Orthorhombic gamma-$CsPbI_3$ Nanocrystals. *ACS Nano* **2023**, *17* (10), 9290−9301.

(9) Pan, G.; Bai, X.; Yang, D.; Chen, X.; Jing, P.; Qu, S.; Zhang, L.; Zhou, D.; Zhu, J.; Xu, W.; Dong, B.; Song, H. Doping Lanthanide into Perovskite Nanocrystals: Highly Improved and Expanded Optical Properties. *Nano Lett.* **2017**, *17* (12), 8005−8011.

(10) Ruan, L.; Zhang, Y. NIR-excitable heterostructured upconversion perovskite nanodots with improved stability. *Nat. Commun.* **2021**, *12* (1), 219.
(11) Dong, Y.; Wang, Y. K.; Yuan, F.; Johnston, A.; Liu, Y.; Ma, D.; Choi, M. J.; Chen, B.; Chekini, M.; Baek, S. W.; Sagar, L. K.; Fan, J.; Hou, Y.; Wu, M.; Lee, S.; Sun, B.; Hoogland, S.; Quintero-Bermudez, R.; Ebe, H.; Todorovic, P.; Dinic, F.; Li, P.; Kung, H. T.; Saidaminov, M. I.; Kumacheva, E.; Spiecker, E.; Liao, L. S.; Voznyy, O.; Lu, Z. H.; Sargent, E. H. Bipolar-shell resurfacing for blue LEDs based on strongly confined perovskite quantum dots. *Nat. Nanotechnol.* **2020**, *15* (8), 668−674.
(12) Yan, D.; Zhao, S.; Wang, H.; Zang, Z. Ultrapure and highly efficient green light emitting devices based on ligand-modified $CsPbBr_3$ quantum dots. *Photon. Res.* **2020**, *8* (7), 1086−1092.
(13) Liang, T.; Liu, W.; Liu, X.; Li, Y.; Wu, W.; Fan, J. In Situ Phase-Transition Crystallization of All-Inorganic Water-Resistant Exciton-Radiative Heteroepitaxial $CsPbBr_3$−$CsPb_2Br_5$ Core−Shell Perovskite Nanocrystals. *Chem. Mater.* **2021**, *33* (13), 4948−4959.
(14) Jiang, G.; Guhrenz, C.; Kirch, A.; Sonntag, L.; Bauer, C.; Fan, X.; Wang, J.; Reineke, S.; Gaponik, N.; Eychmuller, A. Highly Luminescent and Water-Resistant $CsPbBr_3$-$CsPb_2Br_5$ Perovskite Nanocrystals Coordinated with Partially Hydrolyzed Poly(methyl methacrylate) and Polyethylenimine. *ACS Nano* **2019**, *13* (9), 10386−10396.
(15) Ruan, L.; Zhang, Y. Upconversion Perovskite Nanocrystal Heterostructures with Enhanced Luminescence and Stability by Lattice Matching. *ACS Appl. Mater. Interfaces* **2021**, *13* (43), 51362−51372.
(16) Li, Z. J.; Hofman, E.; Li, J.; Davis, A. H.; Tung, C. H.; Wu, L. Z.; Zheng, W. Photoelectrochemically Active and Environmentally Stable $CsPbBr_3/TiO_2$ Core/Shell Nanocrystals. *Adv. Funct. Mater.* **2018**, *28* (1), 1704288.
(17) Zhang, C.; Wang, M.; Shi, J.; Wang, J.; Da, Z.; Zhou, Y.; Xu, Y.; Gaponenko, N. V.; Bhatti, A. S. Preparation of $CsPb(Cl/Br)_3/TiO_2$:Eu^{3+} composites for white light emitting diodes. *Front. Chem.* **2023**, *11*, 1199863.
(18) Zhang, C.; Wang, Z.; Wang, M.; Shi, J.; Wang, J.; Da, Z.; Zhou, Y.; Xu, Y.; Gaponenko, N. V.; Bhatti, A. S. Ultrastable $CsPbBr_3$@$CsPb_2Br_5$@TiO_2 Composites for Photocatalytic and White Light-Emitting Diodes. *ACS Appl. Mater. Interfaces* **2023**, *15* (29), 35216−35226.
(19) Yoon, S.; Seo, M.; Kim, I. S.; Lee, K.; Woo, K. Ultra-Stable and Highly Efficient White Light Emitting Diodes through $CsPbBr_3$ Perovskite Nanocrystals-Silica Composite Phosphor Functionalized with Surface Phenyl Molecules. *Small* **2023**, *19* (7), No. e2206311.
(20) Zhong, Q.; Cao, M.; Hu, H.; Yang, D.; Chen, M.; Li, P.; Wu, L.; Zhang, Q. One-Pot Synthesis of Highly Stable $CsPbBr_3$@SiO_2 Core-Shell Nanoparticles. *ACS Nano* **2018**, *12* (8), 8579−8587.
(21) He, M.; Zhang, Q.; Carulli, F.; Erroi, A.; Wei, W.; Kong, L.; Yuan, C.; Wan, Q.; Liu, M.; Liao, X.; Zhan, W.; Han, L.; Guo, X.; Brovelli, S.; Li, L. Ultra-stable Solution-Processable $CsPbBr_3$-SiO_2 Nanospheres for Highly Efficient Color Conversion in Micro Light-Emitting Diodes. *ACS Energy Lett.* **2023**, *8* (1), 151−158.
(22) Shi, J.; Wang, M.; Wang, H.; Zhang, C.; Ji, Y.; Wang, J.; Zhou, Y.; Bhatti, A. S. Preparation of ultra-stable and environmentally friendly $CsPbBr_3$@ZrO_2/PS composite films for white light-emitting diodes. *Nanoscale* **2022**, *14* (44), 16548−16559.
(23) Du, K.; He, L.; Song, S.; Feng, J.; Li, Y.; Zhang, M.; Li, H.; Li, C.; Zhang, H. In Situ Embedding Synthesis of Highly Stable $CsPbBr_3/CsPb_2Br_5$@PbBr(OH) Nano/Microspheres through Water Assisted Strategy. *Adv. Funct. Mater.* **2021**, *31* (36), 2103275.
(24) Baek, K. Y.; Lee, W.; Lee, J.; Kim, J.; Ahn, H.; Kim, J. I.; Kim, J.; Lim, H.; Shin, J.; Ko, Y. J.; Lee, H. D.; Friend, R. H.; Lee, T. W.; Lee, J.; Kang, K.; Lee, T. Mechanochemistry-driven engineering of 0D/3D heterostructure for designing highly luminescent Cs-Pb-Br perovskites. *Nat. Commun.* **2022**, *13* (1), 4263.
(25) Wang, C.; Wang, Y.; Su, X.; Hadjiev, V. G.; Dai, S.; Qin, Z.; Calderon Benavides, H. A.; Ni, Y.; Li, Q.; Jian, J.; Alam, M. K.; Wang, H.; Robles Hernandez, F. C.; Yao, Y.; Chen, S.; Yu, Q.; Feng, G.; Wang, Z.; Bao, J. Extrinsic Green Photoluminescence from the Edges of 2D Cesium Lead Halides. *Adv. Mater.* **2019**, *31* (33), 1902492.
(26) Ravi, V. K.; Saikia, S.; Yadav, S.; Nawale, V. V.; Nag, A. $CsPbBr_3$/ZnS Core/Shell Type Nanocrystals for Enhancing Luminescence Lifetime and Water Stability. *ACS Energy Lett.* **2020**, *5* (6), 1794−1796.
(27) Vighnesh, K.; Wang, S.; Liu, H.; Rogach, A. L. Hot-Injection Synthesis Protocol for Green-Emitting Cesium Lead Bromide Perovskite Nanocrystals. *ACS Nano* **2022**, *16* (12), 19618−19625.
(28) Ding, L.; Borjigin, B.; Li, Y.; Yang, X.; Wang, X.; Li, H. Assembling an Affinal 0D $CsPbBr_3$/2D $CsPb_2Br_5$ Architecture by Synchronously In Situ Growing $CsPbBr_3$ QDs and $CsPb_2Br_5$ Nanosheets: Enhanced Activity and Reusability for Photocatalytic CO_2 Reduction. *ACS Appl. Mater. Interfaces* **2021**, *13* (43), 51161−51173.
(29) Li, G.; Wang, H.; Zhu, Z.; Chang, Y.; Zhang, T.; Song, Z.; Jiang, Y. Shape and phase evolution from $CsPbBr_3$ perovskite nanocubes to tetragonal $CsPb_2Br_5$ nanosheets with an indirect bandgap. *Chem. Commun. (Camb.)* **2016**, *52* (75), 11296−11299.
(30) Sutton, R. J.; Filip, M. R.; Haghighirad, A. A.; Sakai, N.; Wenger, B.; Giustino, F.; Snaith, H. J. Cubic or Orthorhombic? Revealing the Crystal Structure of Metastable Black-Phase $CsPbI_3$ by Theory and Experiment. *ACS Energy Lett.* **2018**, *3* (8), 1787−1794.
(31) Tang, Y.; Cao, X.; Honarfar, A.; Abdellah, M.; Chen, C.; Avila, J.; Asensio, M. C.; Hammarstrom, L.; Sa, J.; Canton, S. E.; Zheng, K.; Pullerits, T.; Chi, Q. Inorganic Ions Assisted the Anisotropic Growth of $CsPbCl_3$ Nanowires with Surface Passivation Effect. *ACS Appl. Mater. Interfaces* **2018**, *10* (35), 29574−29582.
(32) Zhang, D.; Yang, Y.; Bekenstein, Y.; Yu, Y.; Gibson, N. A.; Wong, A. B.; Eaton, S. W.; Kornienko, N.; Kong, Q.; Lai, M.; Alivisatos, A. P.; Leone, S. R.; Yang, P. Synthesis of Composition Tunable and Highly Luminescent Cesium Lead Halide Nanowires through Anion-Exchange Reactions. *J. Am. Chem. Soc.* **2016**, *138* (23), 7236−7239.
(33) Di, J.; Li, H.; Su, J.; Yuan, H.; Lin, Z.; Zhao, K.; Chang, J.; Hao, Y. Reveal the Humidity Effect on the Phase Pure $CsPbBr_3$ Single Crystals Formation at Room Temperature and Its Application for Ultrahigh Sensitive X-Ray Detector. *Adv. Sci. (Weinh.)* **2022**, *9* (2), 2103482.
(34) Zhu, B. S.; Li, H. Z.; Ge, J.; Li, H. D.; Yin, Y. C.; Wang, K. H.; Chen, C.; Yao, J. S.; Zhang, Q.; Yao, H. B. Room temperature precipitated dual phase $CsPbBr_3$-$CsPb_2Br_5$ nanocrystals for stable perovskite light emitting diodes. *Nanoscale* **2018**, *10* (41), 19262−19271.
(35) Zhang, B.; Goldoni, L.; Zito, J.; Dang, Z.; Almeida, G.; Zaccaria, F.; de Wit, J.; Infante, I.; De Trizio, L.; Manna, L. Alkyl Phosphonic Acids Deliver $CsPbBr_3$ Nanocrystals with High Photoluminescence Quantum Yield and Truncated Octahedron Shape. *Chem. Mater.* **2019**, *31* (21), 9140−9147.
(36) Huang, Z. P.; Ma, B.; Wang, H.; Li, N.; Liu, R. T.; Zhang, Z. Q.; Zhang, X. D.; Zhao, J. H.; Zheng, P. Z.; Wang, Q.; Zhang, H. L. In Situ Growth of 3D/2D ($CsPbBr_3/CsPb_2Br_5$) Perovskite Heterojunctions toward Optoelectronic Devices. *J. Phys. Chem. Lett.* **2020**, *11* (15), 6007−6015.
(37) Zhang, S.; He, J.; Guo, X.; Su, J.; Lin, Z.; Zhang, J.; Guo, L.; Hao, Y.; Chang, J. Crystallization Dynamic Control of Perovskite Films with Suppressed Phase Transition and Reduced Defects for Highly Efficient and Stable All-Inorganic Perovskite Solar Cells. *ACS Materi. Lett.* **2023**, *5* (6), 1497−1505.
(38) Luo, C.; Zhao, Y.; Wang, X.; Gao, F.; Zhao, Q. Self-Induced Type-I Band Alignment at Surface Grain Boundaries for Highly Efficient and Stable Perovskite Solar Cells. *Adv. Mater.* **2021**, *33* (40), No. e2103231.
(39) Fan, M.; Huang, J.; Turyanska, L.; Bian, Z.; Wang, L.; Xu, C.; Liu, N.; Li, H.; Zhang, X.; Zhang, C.; Yang, X. Efficient All-Perovskite White Light-Emitting Diodes Made of In Situ Grown Perovskite-Mesoporous Silica Nanocomposites. *Adv. Funct. Mater.* **2023**, *33* (19), 2215032.

https://doi.org/10.1021/acsami.4c00178
ACS Appl. Mater. Interfaces 2024, 16, 20715−20724

(40) Zhang, J.; Zhang, L.; Cai, P.; Xue, X.; Wang, M.; Zhang, J.; Tu, G. Enhancing stability of red perovskite nanocrystals through copper substitution for efficient light-emitting diodes. *Nano Energy* **2019**, *62*, 434−441.
(41) Jang, E.; Jang, H. Review: Quantum Dot Light-Emitting Diodes. *Chem. Rev.* **2023**, *123* (8), 4663−4692.

https://doi.org/10.1021/acsami.4c00178
ACS Appl. Mater. Interfaces 2024, 16, 20715−20724